

NASA Contractor Report 4490

# Analysis of a High Speed Civil Transport Configuration at Subsonic Flow Conditions Using a Navier-Stokes Solver

Victor R. Lessard  
*ViGYAN, Inc.*  
*Hampton, Virginia*

Prepared for  
Langley Research Center  
under Contract NAS1-18585



National Aeronautics and  
Space Administration  
Office of Management  
Scientific and Technical  
Information Program

**1993**



# **Analysis of a High Speed Civil Transport Configuration at Subsonic Flow Conditions Using a Navier-Stokes Solver**

## **Abstract**

Computations of three dimensional vortical flows over a generic High Speed Civil Transport (HSCT) configuration with an aspect ratio of 3.04 are performed using a thin-layer Navier-Stokes solver. The HSCT cruise configuration is modeled without leading or trailing edge flap deflections and without engine nacelles. The flow conditions, which correspond to tests done in the NASA Langley 8-Foot Transonic Pressure Tunnel (TPT), are a subsonic Mach number of 0.3 and Reynolds number of 4.4 million for a range of angle-of-attack ( $-0.23^\circ$  to  $17.78^\circ$ ). The effects of the farfield boundary location with respect to the body are investigated. The boundary layer is assumed turbulent and is simulated using an algebraic turbulence model. The key features of the vortices and their interactions are captured. Grid distribution in the vortex regions is critical for predicting the correct induced lift. Computed forces and surface pressures compare reasonably well with the experimental TPT data.

## **Symbols**

BL	butt line of model, feet
b	wing span, feet
$C_D$	Drag coefficient
$C_L$	Lift coefficient
$C_M$	Pitching-moment coefficient

$C_P$	Pressure coefficient
CPU	central processing unit
$c$	local wing chord, feet
$\bar{c}$	mean aerodynamic chord, feet
$e$	total energy per unit volume, ft-lb/ft <sup>3</sup>
$F$	inviscid flux in the curvilinear $\xi$ direction
$F_v$	viscous flux in the curvilinear $\xi$ direction
$G$	inviscid flux in the curvilinear $\eta$ direction
$G_v$	viscous flux in the curvilinear $\eta$ direction
G2.5	volume grid with the outer boundary located 2.5 chords away
G6.0	volume grid with the outer boundary located 6.0 chords away
$H$	inviscid flux in the curvilinear $\zeta$ direction
$H_v$	viscous flux in the curvilinear $\zeta$ direction
$J$	Jacobian matrix
$M$	Mach number
MS	model station, feet
$P_a$	Primary vortex attachment line
$P_c$	Primary vortex core
$P_s$	Primary vortex separation line
$P_{T\infty}$	Total pressure in freestream
$Q$	conserved variables
$Re_L$	Reynolds number per unit length
$S_a$	Secondary vortex attachment line
$S_c$	Secondary vortex core
$S_s$	Secondary vortex separation line
$t$	time
TE	trailing edge

TPT	NASA Langley 8-Foot Transonic Pressure Tunnel
$u$	velocity component in the x direction
$v$	velocity component in the y direction
$w$	velocity component in the z direction
$y^+$	nondimensional wall turbulence length
$X$	cartesian coordinate
$Y$	cartesian coordinate
$Z$	cartesian coordinate
$\alpha$	angle-of-attack
$\rho$	density
$\eta$	curvilinear coordinate direction 2 or nondimensional spanwise direction, $Y/(b/2)$
$\xi$	curvilinear coordinate direction 1 or nondimensional streamwise direction, $X/c$
$\zeta$	curvilinear coordinate direction 3 or nondimensional normal direction, $Z/(b/2)$

## **Introduction**

In the past decade, the speed and memory of supercomputers have increased significantly along with advances in algorithm development in computational fluid dynamics (CFD) and advances in interactive grid generation techniques. These improvements have increased the feasibility of using higher order methods (i.e. Navier-Stokes solvers) to compute the flowfield about a complete aircraft configuration for the purpose of aerodynamic analysis and design for all flight regimes. In this investigation, the low subsonic flight ( $Mach=0.3$ ) of a High Speed Civil Transport (HSCT) cruise configuration is studied using a thin-layer Navier-Stokes solver

(CFL3D). This study has evolved from the NASA Langley Research Center High-Speed Airframe Integration Research (HiSAIR) project. The HiSAIR project was formed to improve multidisciplinary analysis, design, and optimization of aircraft systems and to develop a computational environment supportive of such activities. The initial efforts of this program have focused on the design of an HSCT configuration with a cruise speed of Mach 3.0.

In this report, computations are performed to calibrate/validate a Navier-Stokes code with experimental data. The code is given a calibration rating based on the accuracy of the solutions within the known limitations of the code and its users. This rating can then be used to help categorize the code with respect to the computational effort and accuracy needed for its use in the early and latter stages of design work for HSCT configurations. This study is also done to further enhance the understanding of the physics of vortex dominated flow about an HSCT aircraft in subsonic flow conditions. Accurate simulation of the location and the strength of the vortices on such a configuration is crucial to proper design. The induced lift caused by the vortices can result in unfavorable pitch-up characteristics, especially at higher angles-of-attack, which occur at take-off and landing.

The baseline design of the HSCT configuration studied in this report is a blended cranked delta wing/fuselage configuration with blunt leading edges, a modified platypus nose, and highly curved wing-tips. The inboard wing section is swept at  $79.56^\circ$ , and the outboard wing section is swept at  $53.13^\circ$  (fig. 1). Although the HSCT configuration is (in some respects) quite different than a simple slender delta-wing, both exhibit similar vortex flow characteristics. Also both take advantage of the increased nonlinear lift due to the vortices which develop at angles of incidence.

The flow physics of a simple slender delta-wing have been the focus of many computational and experimental investigations. Beginning at or near the apex of a delta-wing (referring to one side of the wing only), the flow separates at the leading edge and a primary vortex forms (see fig. 2). A co-rotating vortex may form due to changes in the leading edge sweep, such as at the crank of a delta wing. If the primary flow is traced from the leading edge, the air flow rolls up and over the primary vortex and impinges on the wing surface along an attachment line

and then flows outward. The induced crossflow accelerates near the wing surface below the core of the vortex, which creates a low pressure region on the surface of the wing. Because of this suction area, an adverse pressure gradient develops outboard of the primary vortex, which causes the boundary layer to separate and form a smaller secondary vortex. This secondary vortex rotates in the opposite direction from the primary leading-edge vortex and may shift outward if the flow changes from laminar to turbulent. This outward shift results from the flow staying attached longer for a turbulent boundary layer. Whether the flow is laminar, turbulent or mixed is dependent on the local Reynolds number. The transitional region can be identified by the movement of the secondary separation line toward the leading edge of the wing (as described above). An interesting note is that the Reynolds number has little or no effect on the resulting forces and moments for a slender sharp edge delta wing [ref. 1]. Furthermore, a tertiary vortex can also form between the primary and secondary vortex depending on the extent of the induced adverse pressure gradients of the primary and secondary vortices.

According to Hummel's [ref. 1] study of the flow field around a delta wing with an aspect ratio of one, the secondary vortex causes the following flow characteristics. First, the secondary vortex causes the core of the leading edge (or primary) vortex to shift toward the wing centerline and to move upwards. This creates an inward shift and a reduction in the primary suction peak. Secondly, the flow that accelerates near the surface in the region of the secondary vortex, leads to another suction peak. The combined effects are small for turbulent boundary layers and larger for laminar boundary layers. Another result from Hummel's [ref. 1] study is that behind a slender delta-wing, a concentrated counter-rotating wake vortex formation develops, which is connected to the primary vortex sheet originating from the leading edge. The combination of the wake vortex and the primary vortex leads to a very complex downwash field behind the wing. It has been suggested by D. Kuchemann [ref. 2] that this may be the cause of relatively high induced drag of slender wings.

Many researchers have computationally investigated the flow around thin delta-wings in subsonic flow using the Euler and the Navier-Stokes equations [refs. 3-11]. These studies showed

that the Euler equations tend to capture the important features of the primary vortices and their interactions with the wing. Trailing-edge vortices in the near wake of the wing also can be modeled. However, secondary and the tertiary vortices and their effects are not captured by the Euler equations. The inability to predict these smaller vortices produce higher than normal suction pressures on the wing surface below the primary vortices. The differences between the Euler solutions and the experimental results were believed to be primarily attributed to the displacement effects of the secondary vortex, which tend to move the primary vortices inboard and up and reduce the primary suction peaks in the pressure distribution. Furthermore, in the Euler case, separation at the leading edge is based on a geometrical singularity (i.e. a sharp leading edge) and not on the effects of viscosity in the boundary layer. The Navier-Stokes equations are needed to resolve the secondary and tertiary vortices and to predict the correct leading edge separation point for cases where there are no geometrical singularities. Accurate simulation of the secondary vortices is essential for tracking the correct position of the primary vortices over the surface of the wing. The Navier-Stokes equations require an increase in computational effort and time compared to the Euler equations. Also, greater inaccuracies in the flow can arise due to insufficient grid clustering and inadequate turbulence modeling.

To reiterate, the objective of this paper is to computationally study the low subsonic flight (Mach=0.3) of an HSCT cruise configuration using a Reynolds averaged, thin-layer Navier-Stokes solver (CFL3D) developed by J.L. Thomas [ref. 12]. The computational results are compared with an experimental data. The CFL3D code was chosen for the calculations because of the favorable computational results obtained by J.L. Thomas et al [ref. 12] on a Hummel low aspect ratio (AR) delta-wing at  $M=0.3$  and  $Re_L=0.95 \times 10^6$  and by S.L. Taylor [ref. 13] for flow over a  $75^\circ$  swept delta-wing at  $M=0.3$  and  $Re_L=0.50 \times 10^6$ .



## Computational Method

The governing equations and the computational method used in the CFL3D code are presented in several references [refs. 14,15]. The governing equations solved are the three-dimensional, Reynolds-averaged, compressible, thin-layer Navier-Stokes equations. They are written in conservation form with the generalized curvilinear coordinates ( $\xi, \eta, \zeta$ ) as:

$$\frac{\partial Q}{\partial t} + \frac{\partial F}{\partial \xi} + \frac{\partial G}{\partial \eta} + \frac{\partial}{\partial \zeta}(H - H_v) = 0 \quad (1)$$

where

$$Q = \frac{1}{J} [\rho \quad \rho u \quad \rho v \quad \rho w \quad e] \quad (2)$$

The coordinates  $\xi, \eta$ , and  $\zeta$  denote the streamwise, spanwise and normal directions, respectively. It is assumed that the  $\zeta$  coordinate lines are nearly orthogonal to the body surface. The symbols  $t, \rho, u, v, w, e$  denote the time, density, cartesian velocity components and total energy, respectively.  $F, G$ , and  $H$  are the inviscid fluxes in the  $\xi, \eta$ , and  $\zeta$  directions respectively, and  $H_v$  is the viscous flux in the  $\zeta$  direction. The viscous fluxes,  $F_v$  and  $G_v$ , are dropped from the governing equations because of the thin-layer assumption, where the dominant effects are assumed to arise from the viscous diffusion normal to the body surface. The state equations are written assuming the ideal gas assumption. Molecular viscosity is calculated using Sutherland's law and Stoke's hypothesis. The Reynolds stresses are modeled using the Baldwin-Lomax turbulence model [ref. 16] with the Degani-Schiff modification [ref. 17]. The governing equations are discretized to be consistent with conservation laws in integral form.

An implicit, finite volume, upwind approach is used to solve the governing equations. Roe's flux-difference splitting [ref. 18] is used to construct the upwind differences for the convective and the pressure terms. The spatial derivatives are written conservatively as a flux balance across the cell, and the shear stress and heat transfer terms are centrally differenced. Spatial approximate factorization and Euler backward integration after linearization in time results

in the solution through 5x5 block-tridiagonal matrix inversions in three directions. An approximate diagonal form of the spatial factors is employed to reduce computational time. The convergence rate is accelerated using a multigrid full-approximation scheme (FAS) [ref. 19] and mesh sequencing for flow initialization. The accuracy of solution algorithm is second-order in space and first-order in time.

### **Grids and Boundary Conditions**

A single body-fitted grid is generated around the HSCT configuration. The wire frame definition of the surface geometry and a representation of the C-O type volume grid created are shown in figure 3. The fine level mesh has 89 cross sections in the streamwise direction (61 cross sections are on the surface of the HSCT), 145 points in the spanwise direction and 65 points in the normal direction. The total number of grid points is 838,825. The average spacing normal to the wing surface varies from  $z/\bar{c} = 1.25 \times 10^{-6}$  near the nose to  $z/\bar{c} = 1.7 \times 10^{-6}$  near the trailing edge. The mean aerodynamic chord ( $\bar{c}$ ) of the model used in the tunnel test is 1.30 feet. The surface spacing distribution corresponds to a nondimensional  $y^+$  value of approximately 0.35. The farfield boundary extends to approximately  $2.5\bar{c}$  in the circumferential and upstream directions and  $2.5\bar{c}$  in the downstream direction. The farfield boundary was increased to  $6.0\bar{c}$  (maintaining the same number of points) to investigate the effects of the outer boundary location with respect to the configuration. There are only minor differences between the solutions using the grids with different farfield boundaries. These differences are thought to be related to the different grid resolutions within the vortex regions. Most of the results presented in this report are from the solutions using the grid with an outer boundary of  $2.5\bar{c}$ . The two grids are designated as G2.5 (farfield boundary at  $2.5\bar{c}$ ) and G6.0 (farfield boundary at  $6.0\bar{c}$ ).

The boundary conditions are specified explicitly in the CFL3D algorithm. The conditions

of no-slip and impermeability with zero-normal-gradient for pressure and temperature are imposed at the solid boundaries. Locally, one-dimensional characteristic boundary conditions are used in the farfield. First-order extrapolation for the conserved variables are used at the downstream boundary. Flow-through boundary conditions are used in the wake region.

## **Results and Discussion**

Three dimensional vortical flows around the HSCT for a range of angle-of-attack ( $-0.23^\circ$ ,  $1.85^\circ$ ,  $5.82^\circ$ ,  $10.14^\circ$ ,  $14.00^\circ$ ,  $17.78^\circ$ ) are computed using the CFL3D code. In this investigation, it is assumed that the entire boundary layer flow is turbulent. The computational results are compared to experimental test results obtained from the NASA Langley 8-Foot Transonic Pressure Tunnel (TPT) [ref. 20]. The upstream flow conditions, corresponding to the tunnel test conditions, are:

$$Re_L = 4.4 \times 10^6, M = .30, T = 580^\circ R$$

where  $Re_L$  is the Reynolds number based on the model's reference length,  $M$  is the freestream mach number, and  $T$  is the freestream temperature. The Navier-Stokes solutions are considered converged when the lift coefficient becomes constant and the residual is decreased by four orders of magnitude. An example plot of the lift coefficient and the residual versus the number of iterations for  $\alpha = 10.14^\circ$  is shown in figure 4; the run procedure along with the run time is given. First, the flow is initialized on two coarser grids, and then the solution is interpolated onto the finest level mesh where iterations are performed until convergence is reached. Multigrid iterations are implemented on the level 2 (medium coarse) mesh and the level 3 (fine) mesh in order to increase the convergence speed. Approximately 11.3 CPU hours on the CRAY-2S computer are used to obtain a converged solution for a single angle-of-attack. Most of the CPU hours are spent on the fine mesh, namely 9.2 CPU hours. Approximately 68 CPU hours were needed in order to obtain the solutions for all 6 angle-of-attack cases.

The effect of the farfield boundary location is a concern when computing the Navier-Stokes equations in subsonic flow. The elliptical nature of the flow dictates that the farfield boundaries should at least be within the freestream flowfield out of the domain of disturbance caused by a body. However, in practice this may not be feasible because the size of the computational domain is limited by run-time memory and CPU costs associated with a particular computer. To study the effects of the domain size, solutions are obtained on two different grids (G2.5 and G6.0), each with a different farfield boundary location. Both grids have the same number of points in each direction.

The computed forces and moments on the HSCT, obtained from both grids, are compared with the experimental TPT results [ref. 20] for a range of angle-of-attack (fig. 5). The forces and moments are calculated about the model's balance reference center, which is 1.60 feet from the nose. The drag polar is shown in figure 5b. All four plots show little differences between the computed results for the G2.5 and the G6.0 grids except at the higher angle-of-attack starting at approximately  $\alpha=10.14^\circ$ . The differences, which occur at the higher angle-of-incidence, are believed to be directly related to the coarseness of the grid in the areas of the primary vortices and not due to the different outer boundary locations. Unfortunately, as the angle of incidence increases, the primary vortices lift further off the body into regions where the grid coarseness becomes a factor in determining the computed strengths of the vortices. This problem may have been partially or entirely eliminated using grid adaption methods. The solution error due to grid coarseness is increased when the G6.0 grid is used since the point distribution moving toward the outer boundary becomes twice as coarse in the normal direction when compared to the G2.5 grid normal distribution. The differences in the primary vortex structures is seen in figure 6, which depicts the normalized total pressure contours obtained from both grids at  $MS=1.30$  and  $\alpha=17.78^\circ$ . Also, note the grid distributions for G2.5 and G6.0 in figure 6. For the lower range of angle-of-attack, both grids yield the same solutions and compare well with experimental results. Since the vortices are near the body surface, the point distribution is adequate. This suggests that the grid resolution plays a greater role in computing the correct forces than does the extent of farfield boundary, within reasonable limits. However, a further grid study is needed to verify this

statement. The results obtained on the G2.5 grid are considered slightly better, and further discussions are directed to these results only.

CFL3D underpredicts the lift coefficient at the higher angle-of-attack by as much as 12% when compared to the experimental data (fig. 5a). This underprediction is believed to be caused by several factors. The coarseness of the grid downstream in the vicinity of the primary vortex core tends to dissipate the strength of the vortex and reduce the induced suction on the surface. Also, on the outboard wing section, the code underpredicts the leading edge suction. This is seen in the pressure coefficient plots at the BL=0.50 station shown in figures 7b, 8b, and 9b.

The computations also overpredict the pitching moment coefficients at most angles-of-attack, when compared to the experimental data (fig. 5a). However, the moment curve trends are similar. The experimental pitching-moment is approximately constant up to  $\alpha=5^\circ$ , between  $\alpha=5^\circ$  and  $\alpha=10^\circ$  the pitching-moment increases nonlinearly due to the induced lift caused by the vortices and for  $\alpha>10^\circ$  the pitching-moment increases linearly. The predicted moment curve shows that the nonlinear effects of the vortices begin to appear at  $\alpha=4^\circ$ . However, unlike experiment, the moment linearly increases for  $\alpha<4^\circ$ . The overprediction is believed to be directly related to an underestimation of the primary vortex lift near the trailing edge at the higher angle-of-attack due to grid coarseness in the vicinity of the vortex core and an underestimation of the leading edge suction on the outboard wing section. A reduction of the computed lift at the trailing edge and on the outboard wing, which lies behind the moment center, produces an increase in pitch-up moment. The computed drag coefficient compares well with the experimental drag except between  $\alpha=10.14^\circ$  and  $14.00^\circ$  where the computed drag is slightly lower (fig. 5b). The calculated drag polar compares well up to  $\alpha=10.14^\circ$  where the computed lift starts to diverge from the experimental lift (fig. 5b).

The computed versus the experimental surface pressure coefficients at three model stations (MS=0.74, 1.30, 1.72) and one butt line station (BL=0.50) for  $\alpha=10.14^\circ$ ,  $14.00^\circ$ ,  $17.78^\circ$  are shown in figures 7, 8 and 9, respectively. At each model station the nondimensional  $\eta$  parameter is defined as the distance from the body centerline divided by the local semispan. At the butt-line

station, the nondimensional  $\xi$  parameter is defined as the distance from the leading edge divided by the local chord. Considering the complexities of this multiple vortical flow, the computed surface pressures are in good agreement with the measured data for the model stations. The locations of the primary vortices appear to be correct and evidence of secondary vortices are noted by a slight suction peak in the computed pressures outboard of the primary peak (figs. 7a, 8a, and 9a). However, it is unclear whether secondary separation occurred in the test because of the limited number of pressure ports at the leading edge. The suction peaks of the primary and secondary vortices increase with increase in angle-of-attack. There is no indication of a tertiary vortex in the computational or experimental pressure data. On top of the fuselage, prior to the wing juncture at approximately  $\eta=0.15$ , another suction peak occurs. This low pressure region is caused by the induced crossflow velocity, which increases around the curved surface of the fuselage. For most of the angles-of-attack considered, the calculations tend to overpredict this suction peak. Downstream of the crank at  $MS=1.72$ , the computed pressures show a high suction peak near the leading edge (figs. 7b, 8b, and 9b). This is a strong crank vortex, which starts to form at the vertex of the outboard wing. The induced suction of the crank vortex also increases with an increase in angle-of-attack. Unfortunately, there is an inadequate amount of measured data in this region to determine the accuracy of the vortex strength. The predicted pressure distribution on the outboard wing at  $BL=0.50$  do not compare well with the measured data (figs. 7b, 8b and 9b). The measured suction peak near the leading edge decreases as the angle-of-attack increases; the computed peak is always less and stays approximately constant.

Surface and off-body computational results for several angles-of-attack are shown in figures 10 through 16. Figure 10 shows limiting streamlines on the upper surface of the wing, figures 11-13 shows off-body total pressure contours and figures 14-16 shows cross sectional velocity vectors. The limiting streamlines on the upper surface of the HSCT model for  $\alpha=-0.23^\circ$ ,  $10.14^\circ$ , and  $17.78^\circ$  are depicted as black lines in figure 10. Although there are no experimental surface oil flow data for comparisons, the computed steamlines are considered reasonable. On the outboard wing section for  $\alpha=-0.23^\circ$ , the streamlines are aligned with the freestream flow. On the

inboard section along the smooth juncture between the fuselage and wing, the streamlines converge to a crossflow separation line. The two converging flows do not form a vortex but turn downstream at the crossflow separation point (this is known from studying crossflow velocity vectors which are not shown). At  $\alpha=10.14^\circ$  the flow separates at the leading edge and forms a primary vortex, which reattaches at the centerline (figs. 10, 15). At approximately 1/3 of the distance downstream from the nose, the streamlines near the centerline converge along the wing/fuselage blended juncture. The velocity vectors (not shown) at this location indicates a small separation bubble at the juncture. The streamlines on the inboard wing depict a secondary vortex separation line, which merges with the secondary reattachment line before the crank vertex. This reattachment line is located closest to the leading edge. The merging of the separation and reattachment lines indicates that the secondary vortex dissipates before reaching the crank. On the outboard wing section, the flow is almost entirely in the spanwise direction. A vortex develops at the crank and is fed by flow from the leading edge and from the induced flow of the primary vortex. This phenomena is not apparent in the surface flow streamlines. However, the development of the crank vortex is easily seen from the cross sectional total pressure and velocity vector plots in figures 12 and 15, respectively. An adverse pressure gradient causes another secondary vortex to develop approximately midspan on the outboard wing section. This secondary vortex follows the curved leading edge. Again, the secondary reattachment line lies outboard of the separation line. At  $\alpha=17.78^\circ$  the limiting streamlines are similar to those at  $\alpha=10.14^\circ$ . As the angle-of-attack is increased, the location of the dissipation of the secondary vortex on the inboard wing section moves further downstream near the crank. The location of the inboard secondary separation line is approximately the same; however, for the higher angle-of-attack the secondary reattachment line moves further outboard toward the leading edge. This indicates that the inboard secondary vortex grows larger and gains strength at the higher angle-of-attack. The extent of the spanwise flow increases from the inboard wing to the outboard wing section (near the trailing edge). This increase in the spanwise flow increases the local angle-of-attack on the outboard wing.

The predicted normalized total pressure contours at the three model stations ( $MS=0.74$ ,

1.30, 1.72) and at the trailing edge (TE) for  $\alpha=5.8^\circ$ ,  $10.14^\circ$  and  $17.78^\circ$  are shown in figures 11, 12, and 13. The projected paths of the primary and crank vortices are indicated by dashed lines. As can be seen, the primary vortex turns outboard downstream of the crank. This is caused by the spanwise flow on the outboard wing. The minimum total pressures outside of the boundary layer occur within the vortical core. The amount of total pressure loss is directly related to the vortex strength; i.e., the greater the vortex strength the greater the pressure loss. The strength of the primary vortex increases as the angle-of-attack increases. (Note the lower pressure value in the primary vortex core for  $\alpha=17.78^\circ$ , fig. 13). Also the cores of the primary and crank vortices move farther off the body as the angle-of-attack is increased. As mentioned earlier, for each angle-of-attack considered, a weak secondary vortex, which is near the leading edge is seen at  $MS=0.74$  and 1.30. For the lower angle-of-attack, the boundary layer stays attached longer in turbulent flow; therefore, the secondary vortex is weaker. At  $MS=1.72$ , the secondary vortex has diminished and the crank vortex begins to form. This flow characteristic is substantiated in figure 10. For the lower angle-of-attack, the primary vortex and crank vortex is seen at the trailing edge of the wing (figs. 11, 12). A crank vortex appears to have partially formed for  $\alpha=17.78^\circ$  (Fig. 13). Velocity vectors in a crossflow plane ( $MS=1.92$ , positioned downstream of the crank) are shown in figures 14, 15, and 16. The nondimensional parameters  $\zeta$  and  $\eta$  are the normal and spanwise distances divided by the model station's local semispan. The primary vortex and crank vortex are clearly depicted for  $\alpha=5.82^\circ$  and  $10.14^\circ$ . However, figure 16 does not reveal a crank vortex which was thought to have formed at  $\alpha=17.78^\circ$ . The crossflow velocity vectors suggest that the crank vortex is engulfed by the primary vortex. The low pressure region (at the trailing edge) shown in figure 13 is not indicative of a crank vortex but rather due to the flow sharply turning into the primary vortex.



## **Conclusions**

The Navier-Stokes solver (CFL3D) captured all of the salient features of the complex vortical flow around the High Speed Civil Transport crank delta wing model. In general the computed surface pressures compared well with the experimental data, which suggests that the order of the magnitude of the strengths and positions of the primary and second vortices were correctly simulated at the particular model stations. At the lower angle-of-attack, the lift and drag forces compared well with experimental data. The prediction of the pitching-moment was not good but followed experimental trends. The solutions on the two different grids suggests that the computed aerodynamic forces and moments for a cranked delta wing are highly dependent on grid resolution in the area of the vortices. A single grid is not satisfactory for capturing the correct vortex strengths at all angles-of-attack. A preferred method would be to use a grid adaption technique or multiple grids. It is believed that the CFL3D code is a valuable tool for the analysis of delta wings in low speed flow. However, the amount of CPU time needed for a complex configuration deters its use for preliminary parametric design studies.

Research was supported by the National Aeronautics and Space Administration under Contract No. NAS1-18585.

## **References**

1. Hummel, D.: *On the Vortex Formation Over a Slender Wing at Large Angles of Incidence*, AGARD-CP-247, October 1978.
2. Kuchemann, D.: *Entwicklungen in der Traflugeltheorie. 11. Ludwig-Prandtl-Gedachtnis-Vorlesung*. Jb. 1967 der WGLR, 11-22.
3. Murman, E.M. and Rizzi, A.: *Applications of Euler Equations to Sharp Edge Delta Wings With Leading Edge Vortices*, AGARD-CP-412, April 1986.

4. Rizzi, A. and Purcell, C.J.: *Numerical Experiment with Inviscid Vortex-Stretched Flow Around a Cranked Delta Wing: Subsonic Speed*, AIAA-85-4080, October 1985.
5. Berg, J.I. van den and Hoeijmakers, H.W.M.: *Study Into the Limits of An Euler Equation Method Applied to Leading-Edge Vortex Flow*, NLR TP 90368 U, 1990.
6. Hoeijmakers, H.W.M.; Jacobs, J.M.J.W.; and Berg, J.I. van den: *Numerical Simulation of Vortical Flow Over a Delta Wing at Subsonic and Transonic Speeds*, ICAS Paper 90-3.3.3, 1990.
7. Hoeijmakers, H.W.M. and Berg, J.I. van den: *Application of an Euler-Equation Method to a Sharp-Edge Delta-Wing Configuration with Vortex Flow*, AIAA -91-3310, 1991.
8. Rizzi, A.; Muller, B.; and Purcell, C.J.: *Comparison of Euler and Navier-Stokes Solutions for Vortex Flow Over a Delta Wing*, AIAA-87-2347, 1987.
9. Rizzetta, D.P. and Shang, J.S.: *Numerical Leading-Edge Vortex Flows*, AIAA-84-1544, 1984.
10. McMillin, S.N.; Thomas, J.L.; and Murman, E.M.: *Navier-Stokes and Euler Solutions for Lee-side Flows Over Supersonic Delta Wings*, NASA TP-3035, Dec. 1990.
11. Hsu, C.-H. and Liu, C.H.: *Navier-Stokes Computation of Flow Around a Rounded-EDGE Double-Delta Wing*, AIAA-88-2560-CP, 1988.
12. Thomas, J.L.; Taylor, S.L.; and Anderson, W.K.: *Navier-Stokes Computations of Vortical Flows Over Low Aspect Ratio Wings*, AIAA-87-0207, 1987.
13. Taylor, S.L.; Kjelgaard, S.O.; Weston, R.P.; Thomas, J.L.; and Sellers III, W.L.: *Experimental and Computational Study of the Subsonic Flow About a 75° Swept Delta Wing*, AIAA -87-2425, 1987.
14. Thomas, J.L. and Newsome, R.: *Navier-Stokes Computations of Lee-Side Flows over Delta Wings.*, AIAA-86-1049, 1986.
15. Vatsa, V.N.; Thomas, J.L.; and Wedan, B.W.: *Navier-Stokes Computations of Prolate Spheroids at Angle of Attack.*, AIAA-87-2627-CP, 1987.
16. Baldwin, B.S. and Lomax, H.: *Thin Layer Approximation and Algebraic Model for Separated Turbulent Flows*, AIAA - 78 -257, 1978.

- 17 Degani, D. and Schiff, L.B.: *Computation of Supersonic Viscous Flows Around Pointed Bodies at Large Incidence*, AIAA - 83 - 0034, January 1983.
18. Roe, P.L.: *Characteristic-Based Schemes for Euler Equations*, Annual Review of Fluid Mechanics, Vol. 18, 1986, pp 337-365.
19. Anderson, W.K. and Thomas, J.L.: *Multigrid Acceleration of the Flux Split Euler Equations*, AIAA-86-0274, 1986.
- 20 Belton, P.S. and Campbell, R.L.: *Experimental Study of a Generic High Speed Civil Transport-Tabulated Data*, NASA Technical Memorandum 104216, March 1992.

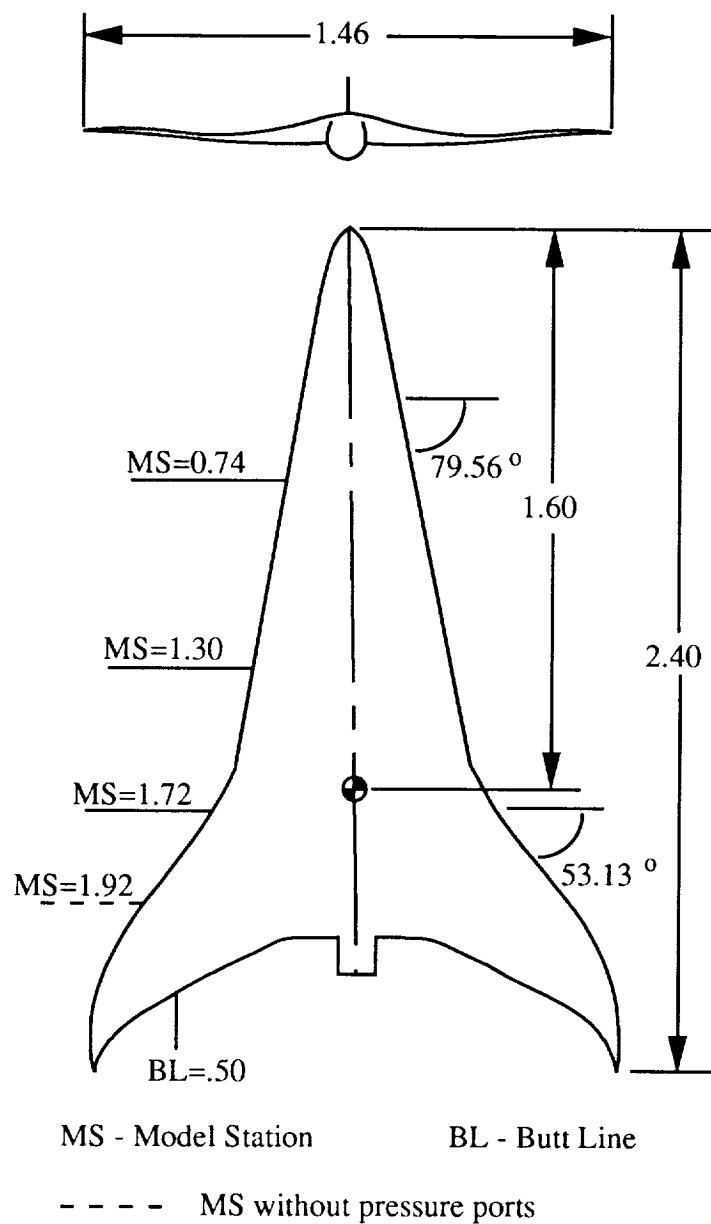
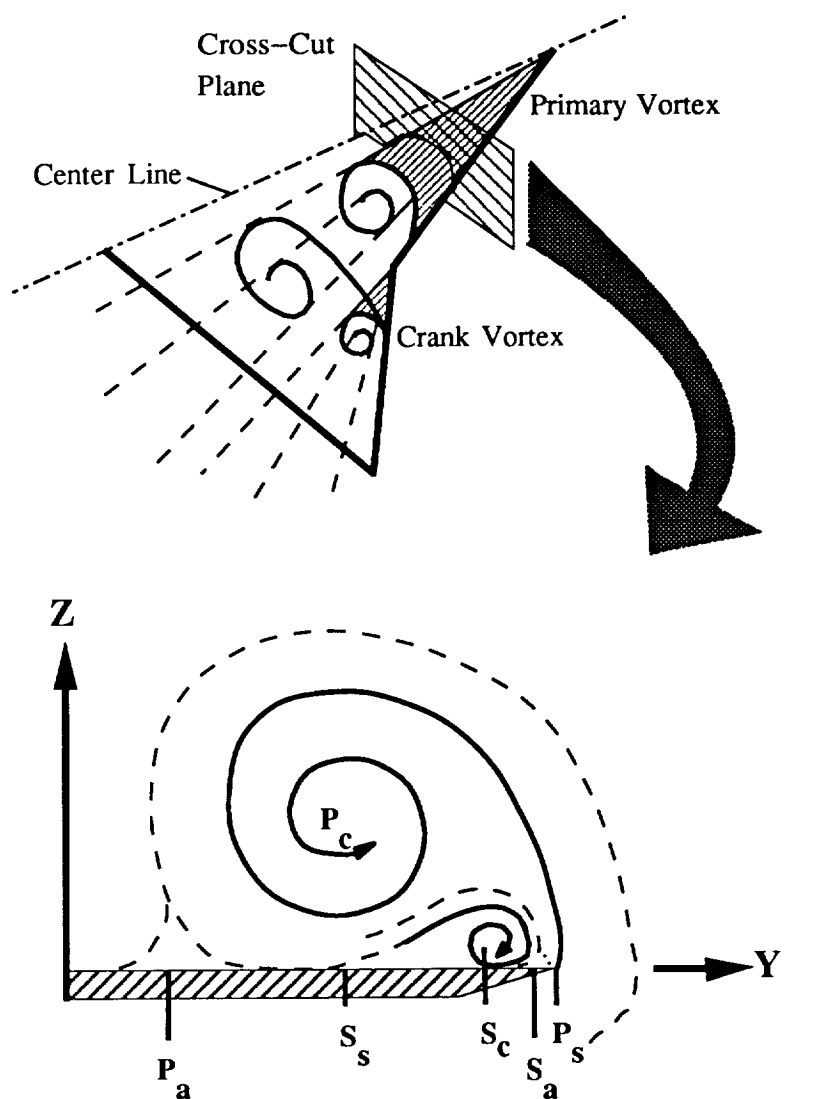


Figure 1. Planform view of the High Speed Civil Transport configuration with model station and butt line pressure port locations. All linear dimensions are in feet.

## Cranked Delta Wing



### Nomenclature

P – Primary Vortex

S – Secondary Vortex

### Subscripts

c – core

a – Attachment Line

s – Separation Line

### Key

— Vortical Flow

- - - Induced Flow

Figure 2. Vortical flow characteristics of a cranked delta wing.

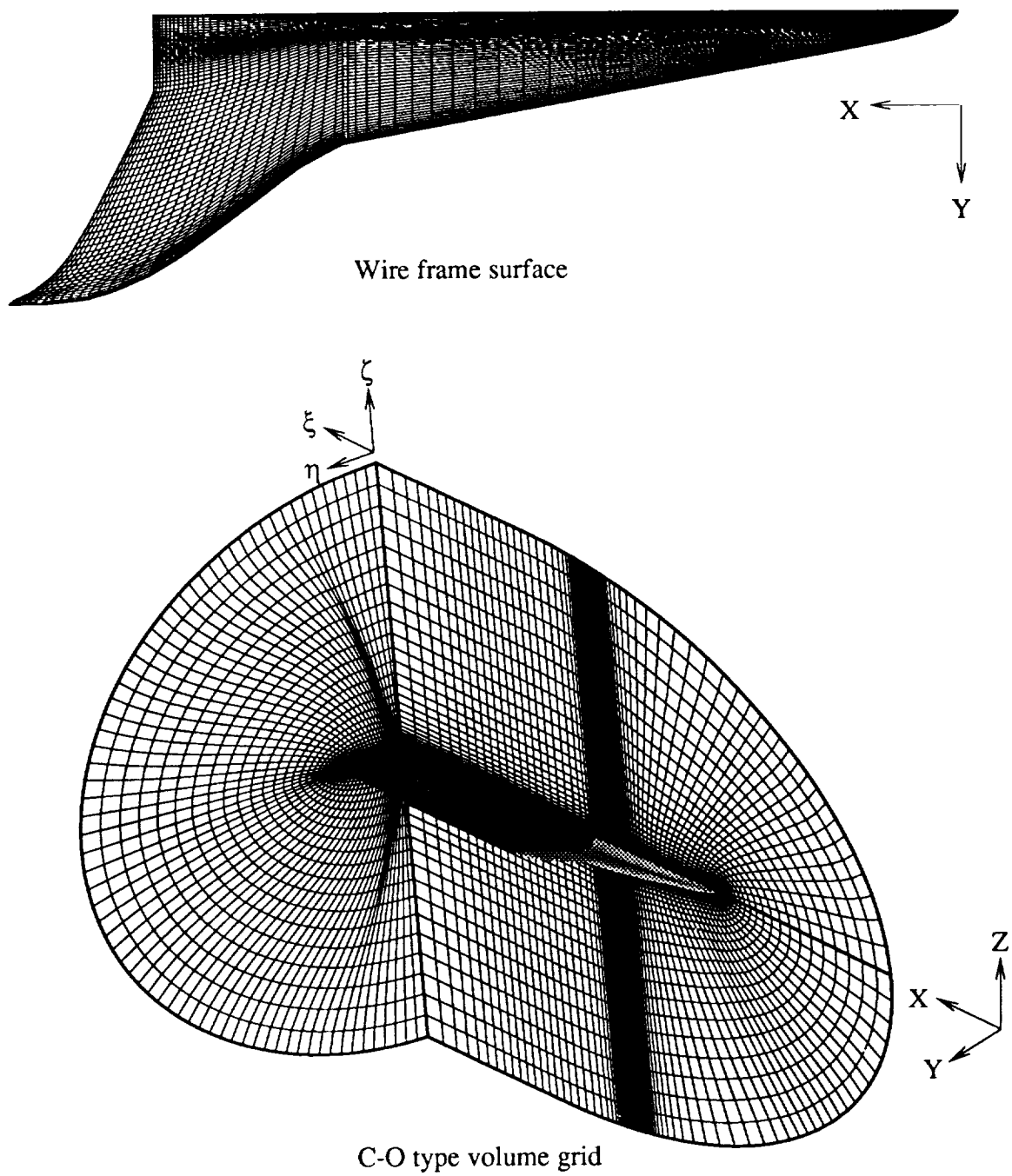
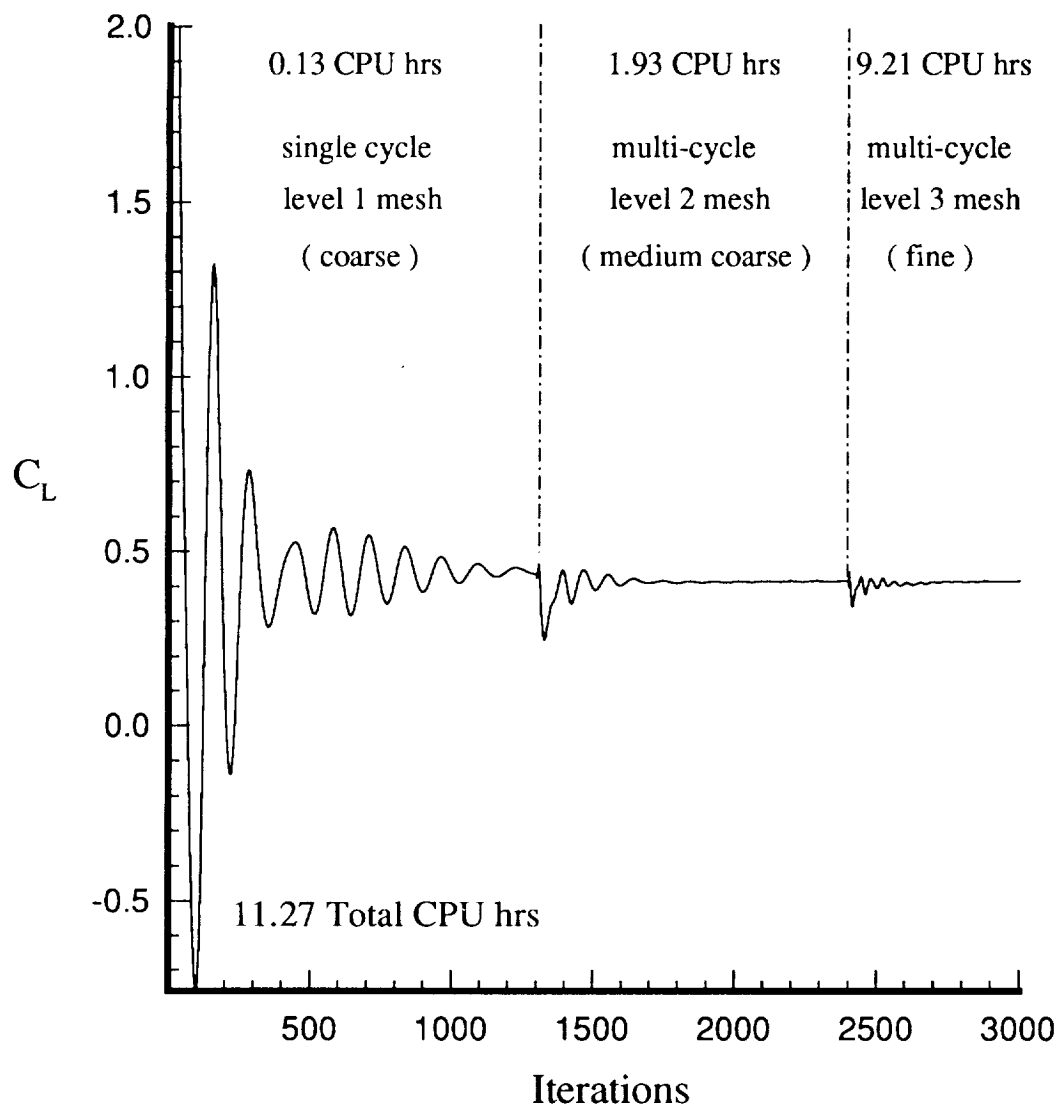
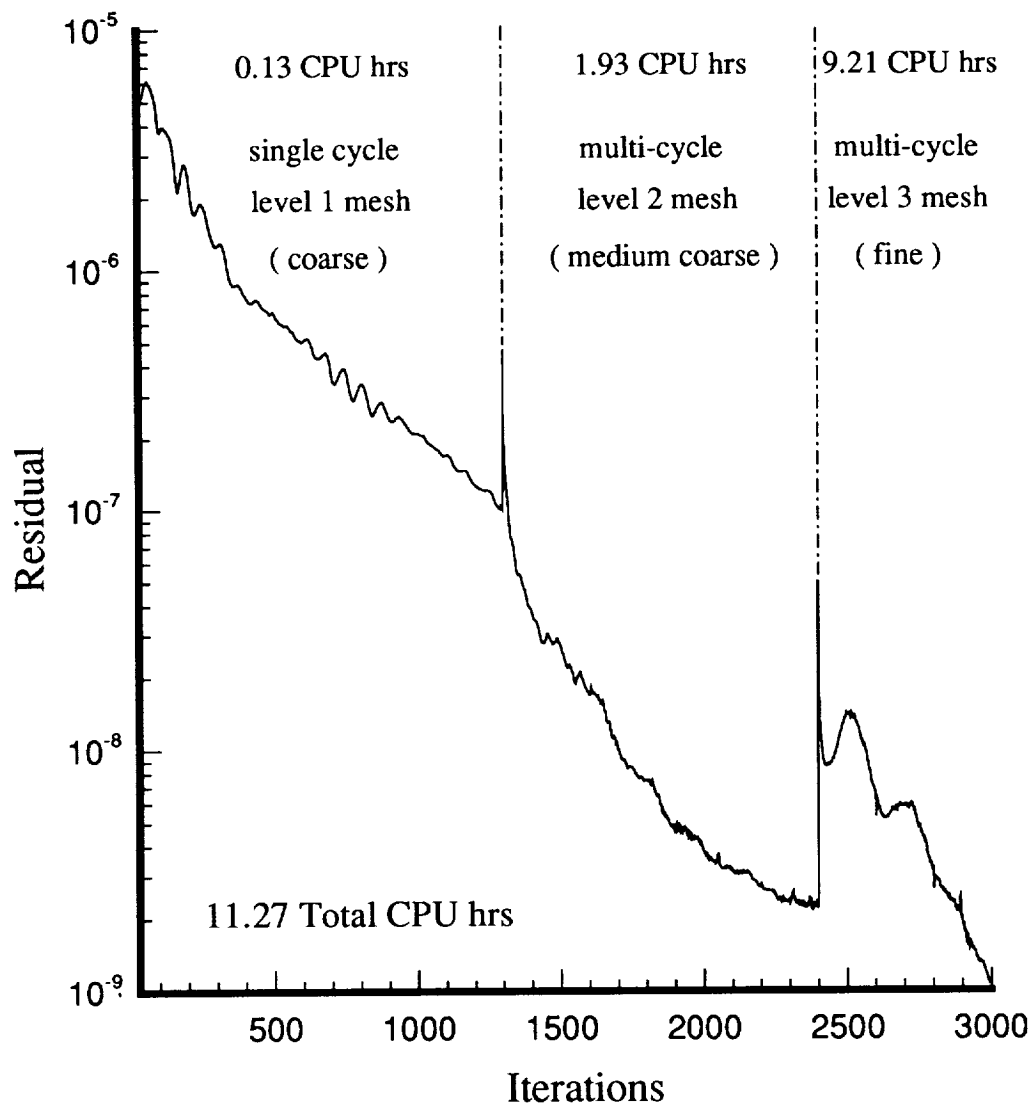


Figure 3. The computational grid for the HSCT model.



(a) Lift history

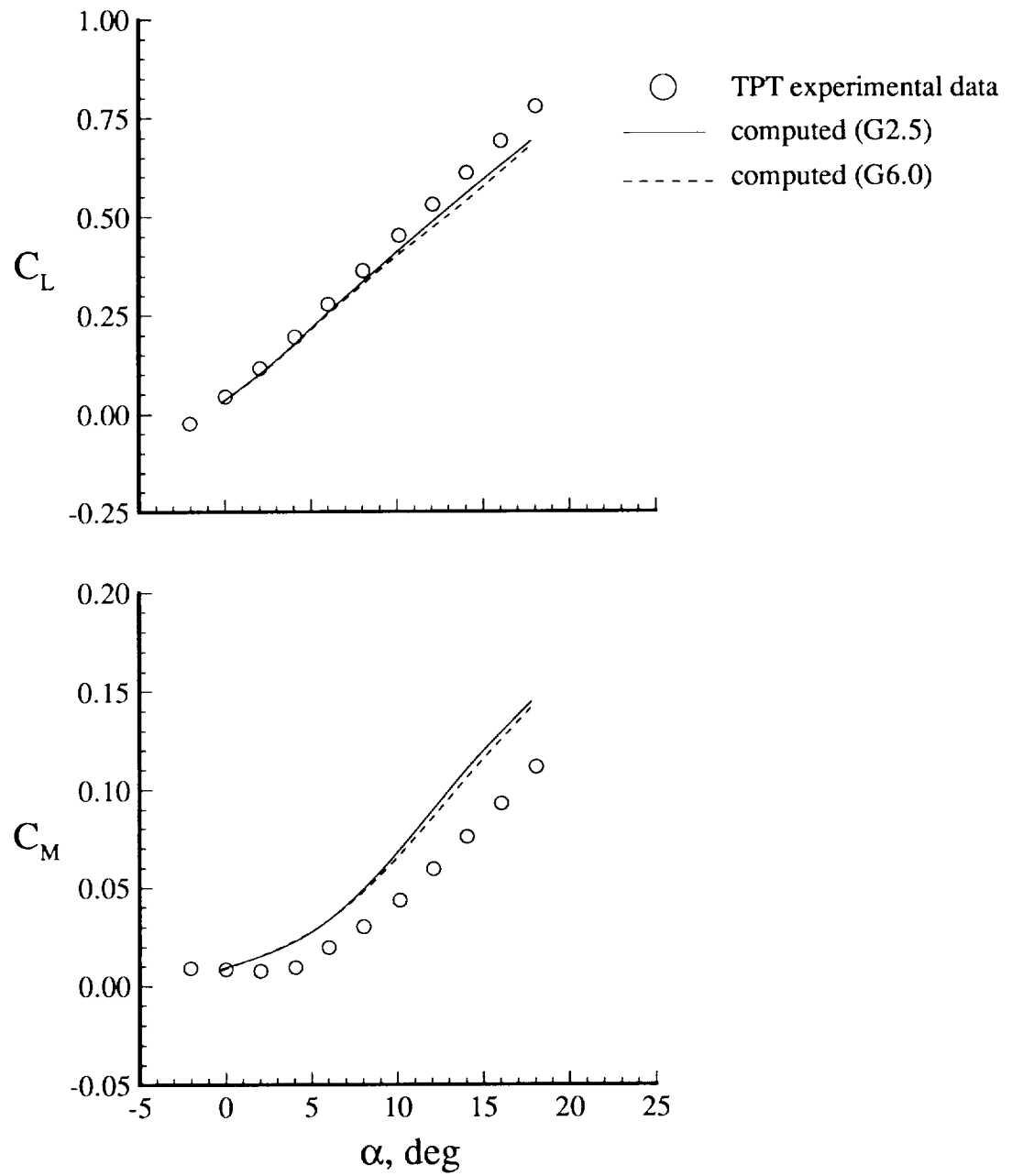
Figure 4. Convergence history of the HSCT solution at  $\alpha=10.14^\circ$ .



(b) Residual history

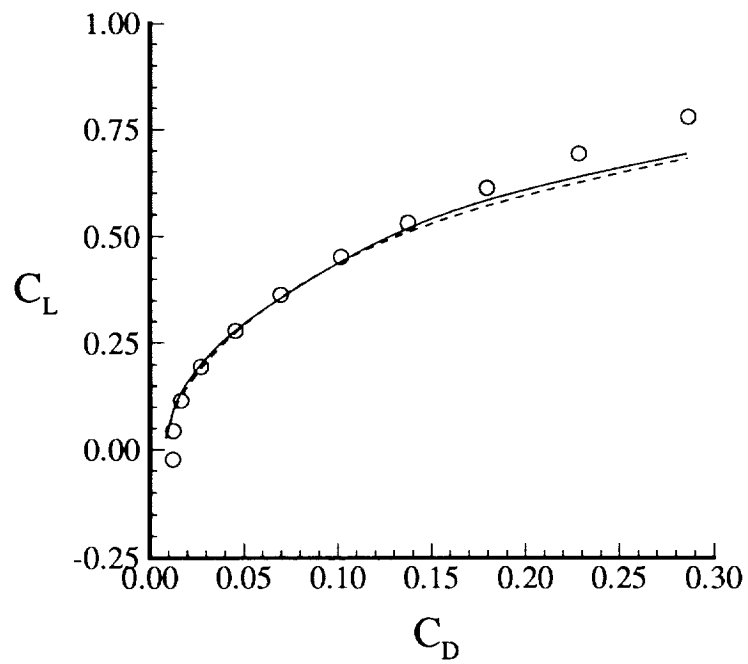
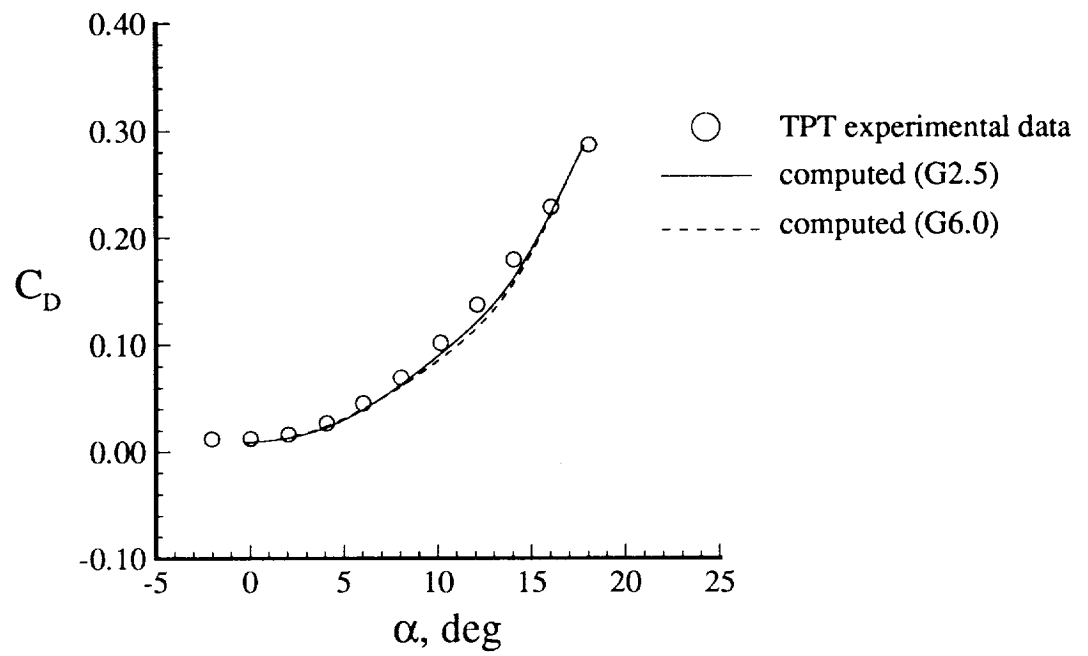
Figure 4. Concluded





(a) Lift and pitching moment curves

Figure 5. Comparison of TPT experimental data with CFD solutions.



(b) Drag curve and drag polar

Figure 5. Concluded.

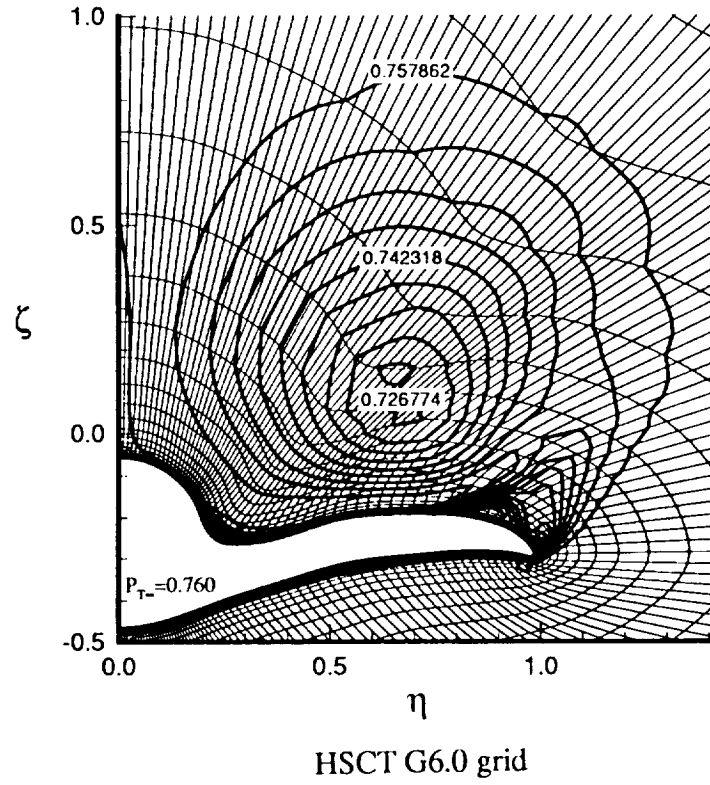
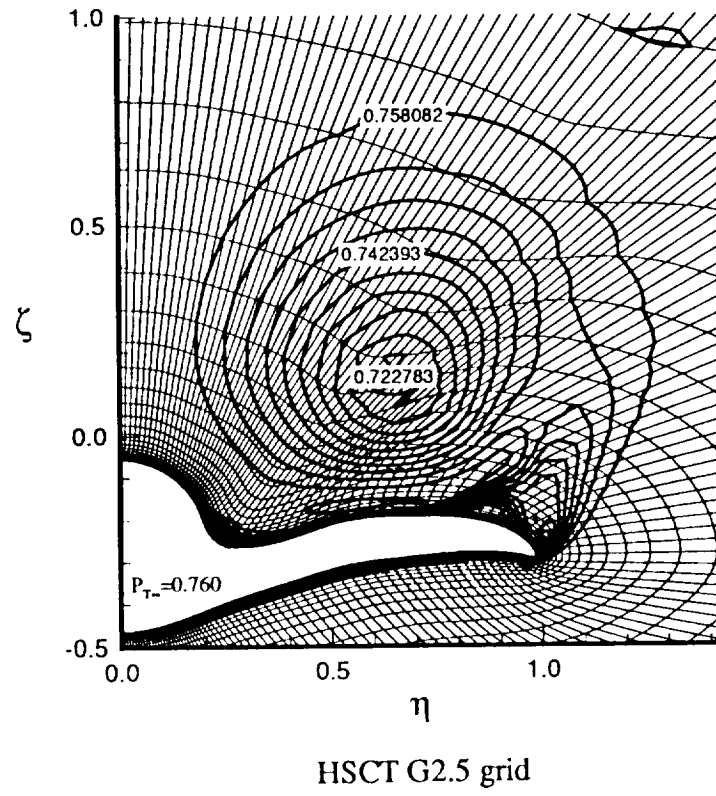
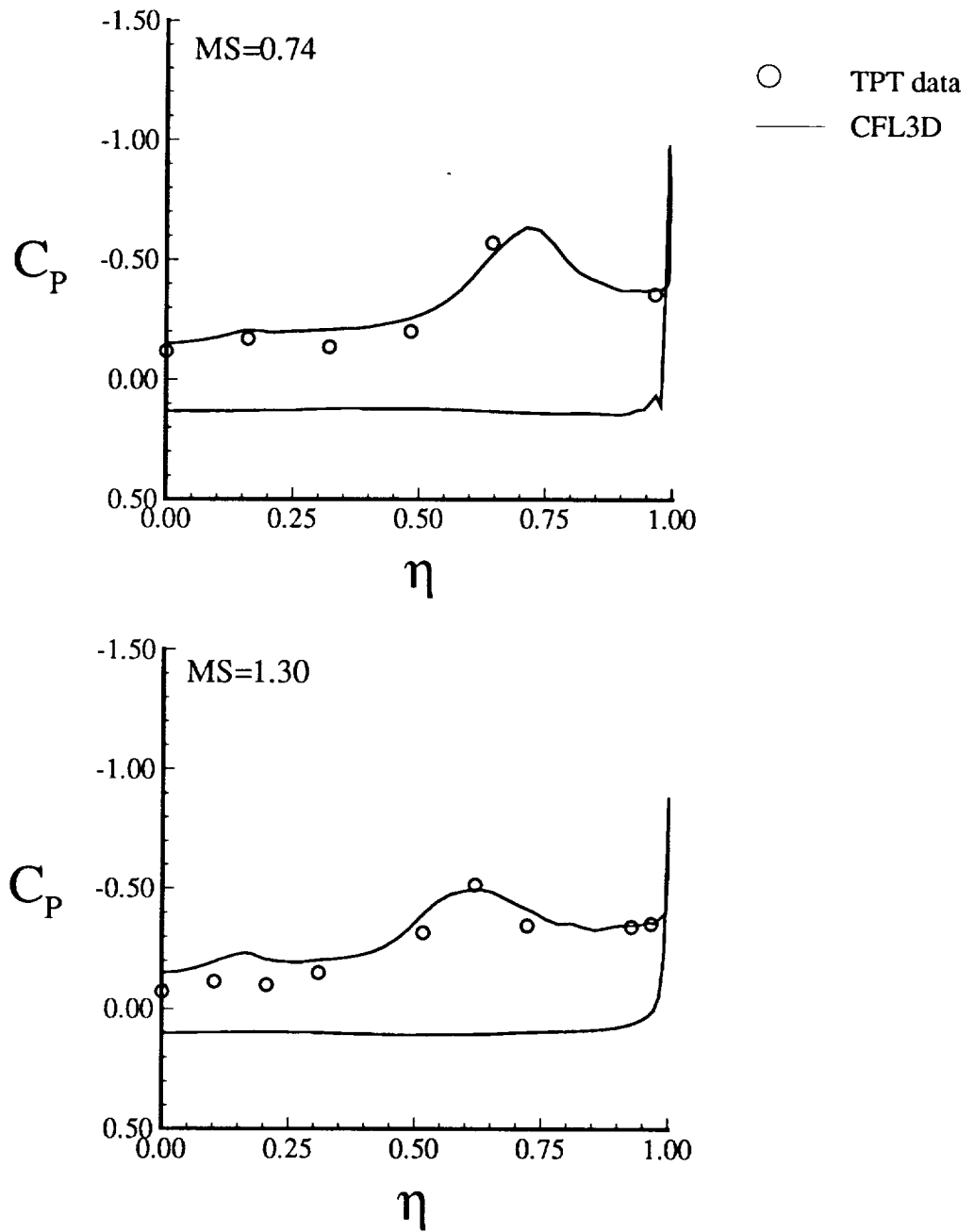
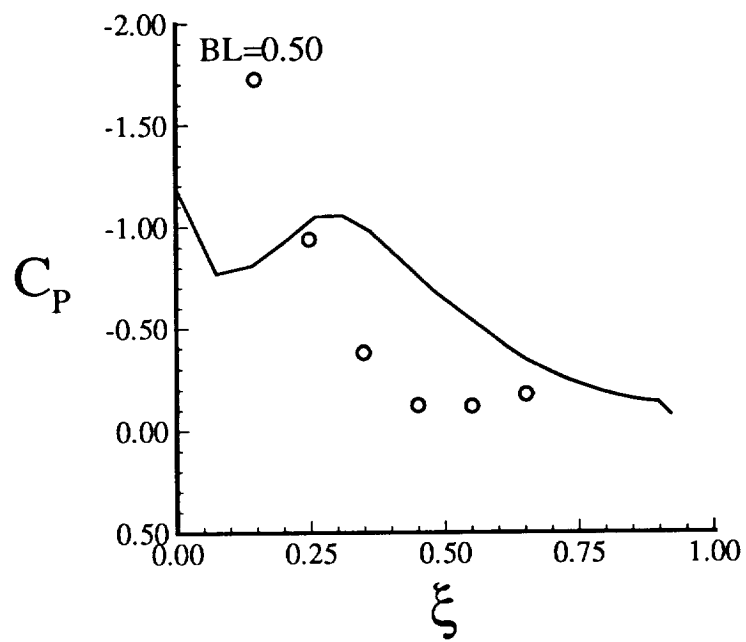
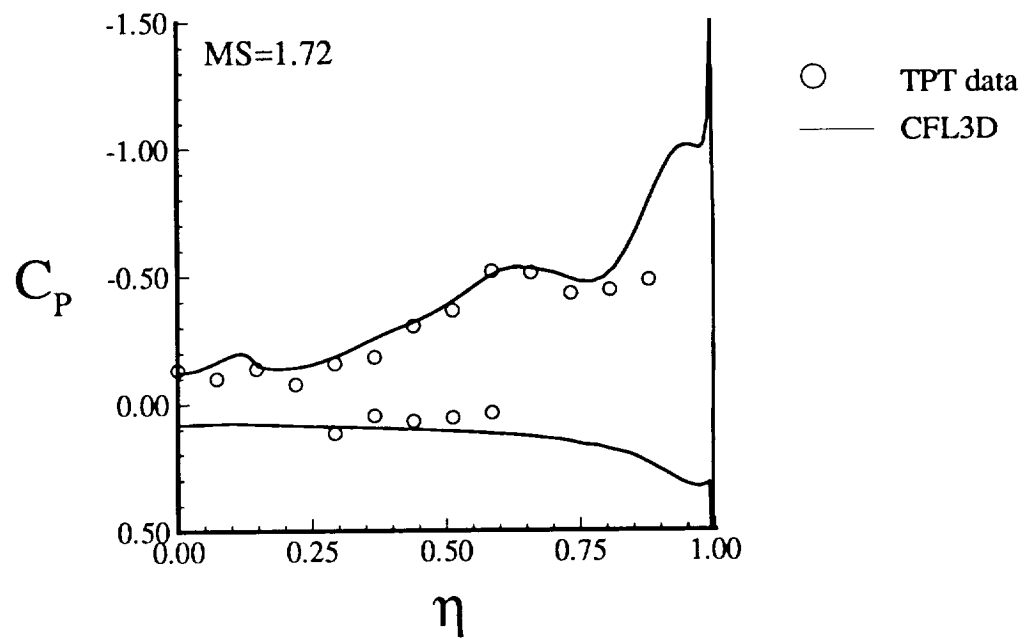


Figure 6. Normalized total pressure contours overlaid on the grid at MS=1.30 for  $\alpha=17.78^\circ$ .



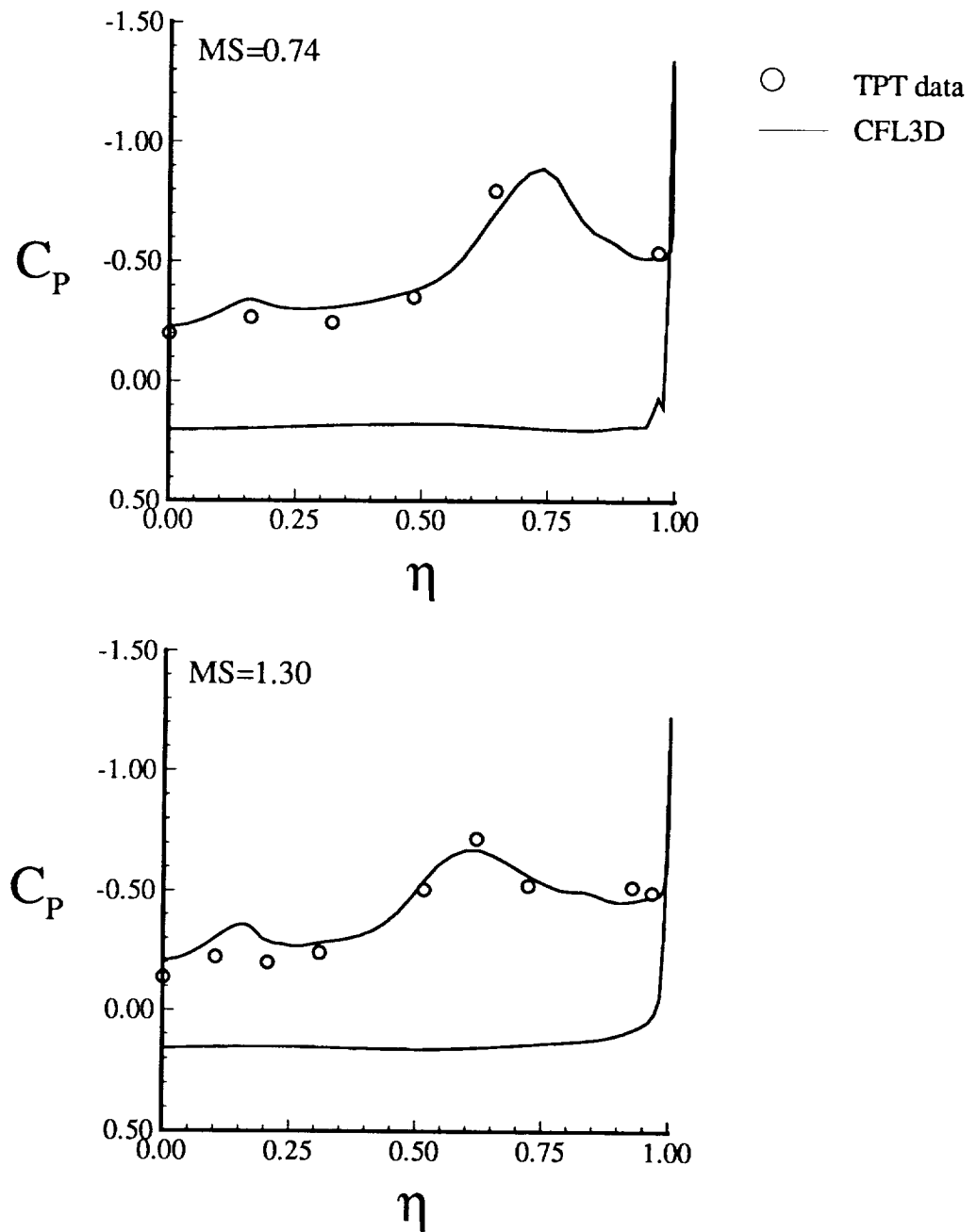
(a) Model stations .74 and 1.30

Figure 7. Comparison of experimental and predicted surface pressures on the HSCT model for  $\alpha=10.14^\circ$ .



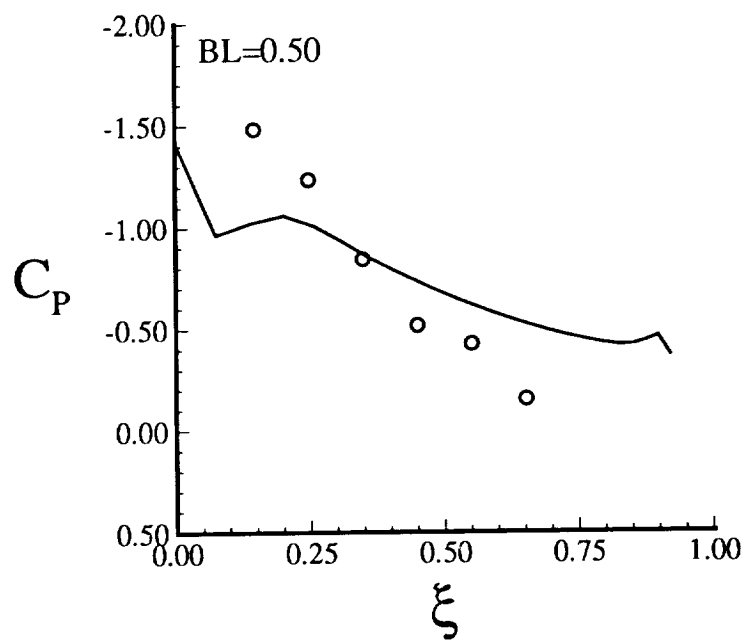
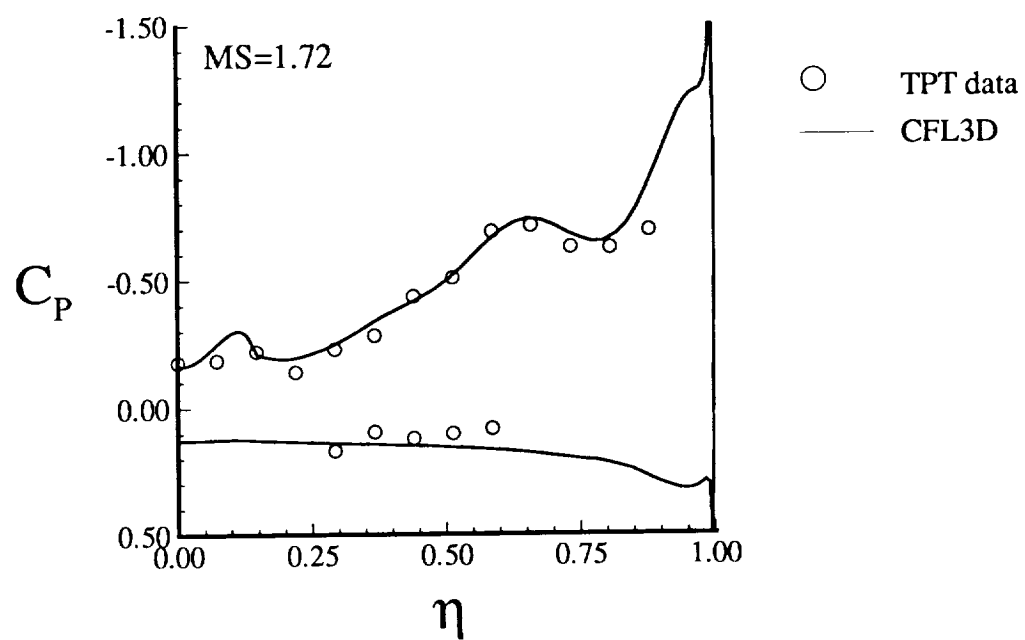
(b) Model station 1.72 and Butt Line .50

Figure 7. Concluded.



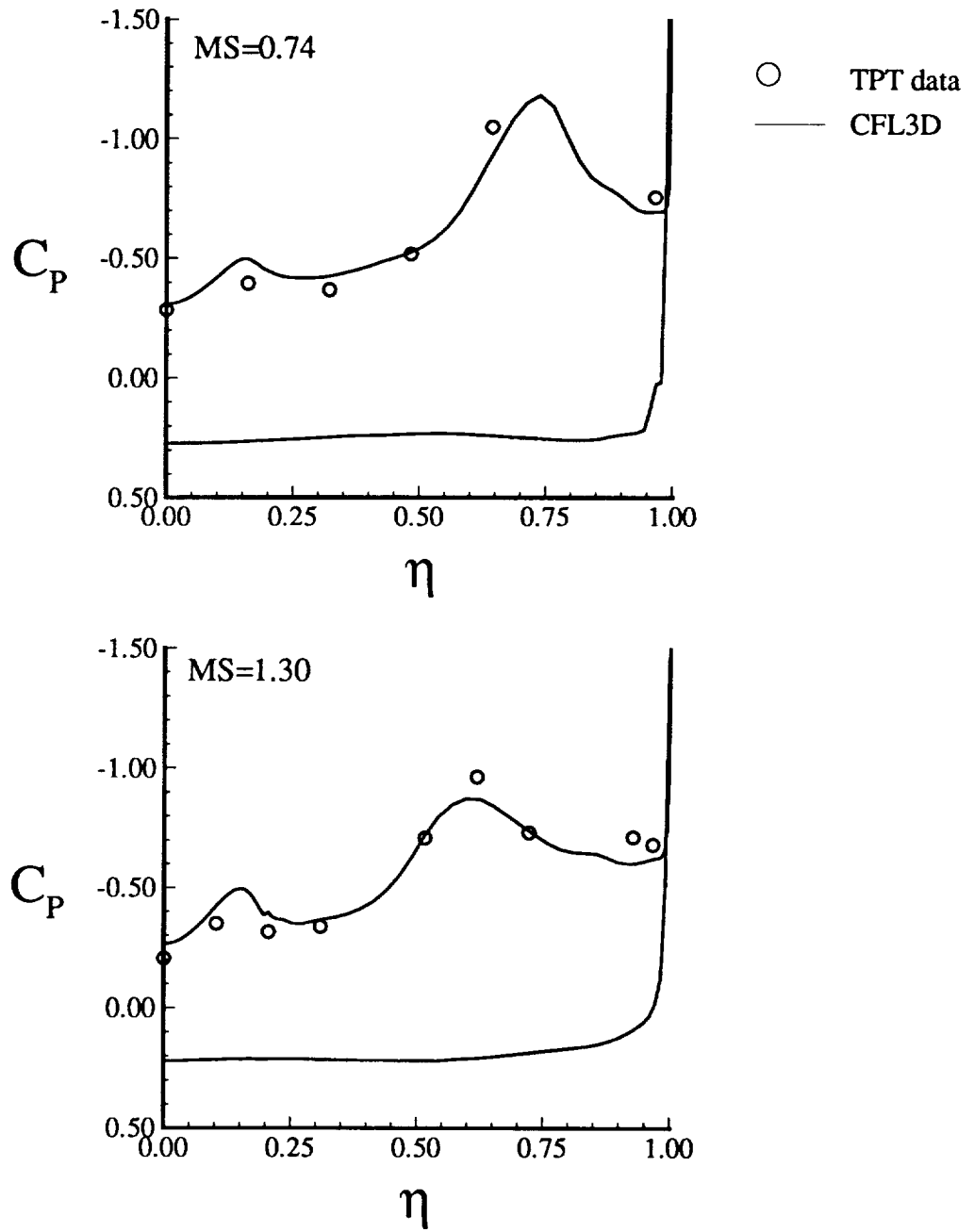
(a) Model stations .74 and 1.30

Figure 8. Comparison of experimental and predicted surface pressures on the HSCT model for  $\alpha=14.00^\circ$ .



(b) Model station 1.72 and Butt Line .50

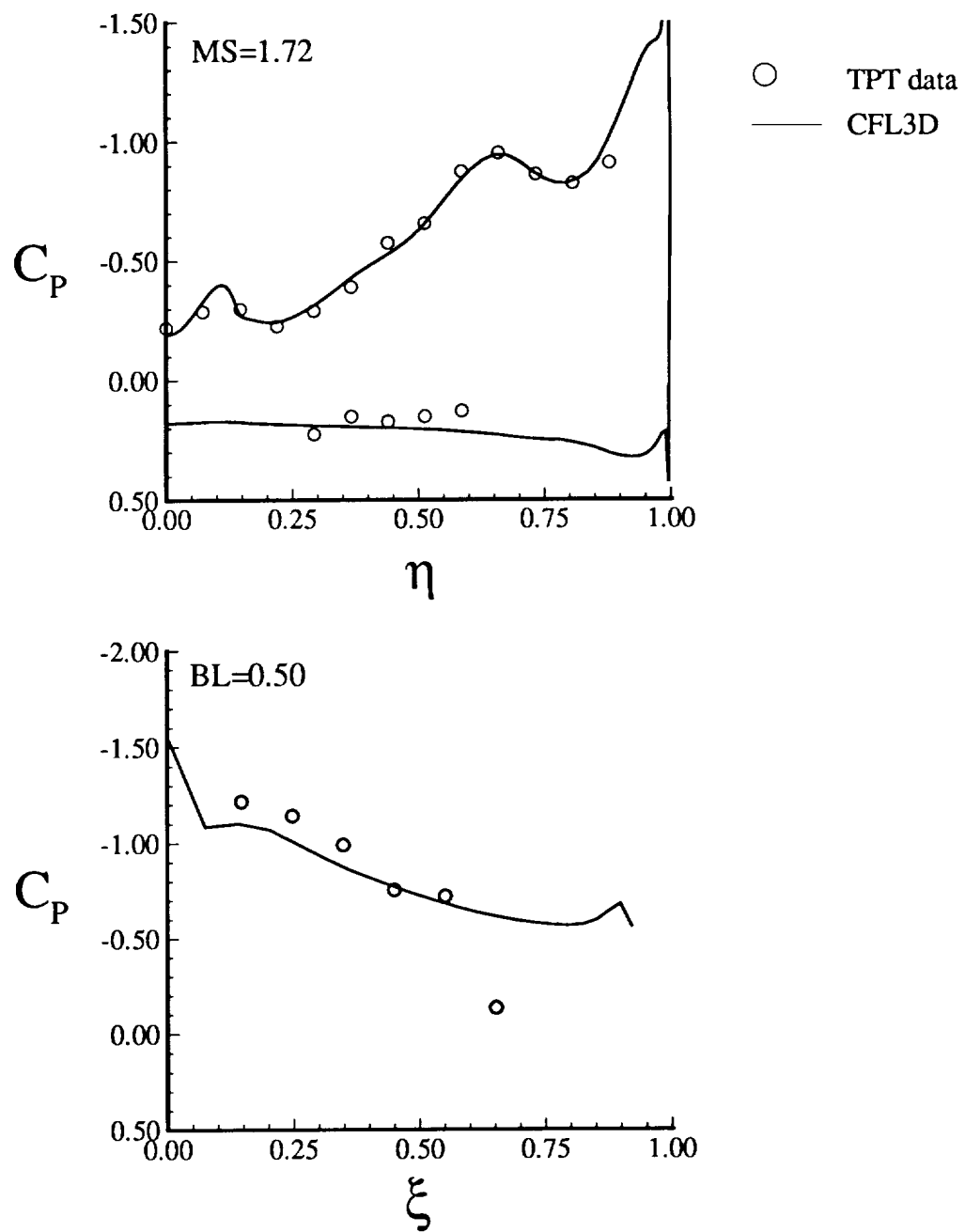
Figure 8. Concluded.



(a) Model stations .74 and 1.30

Figure 9. Comparison of experimental and predicted surface pressures on the HSCT model for  $\alpha=17.78^\circ$ .



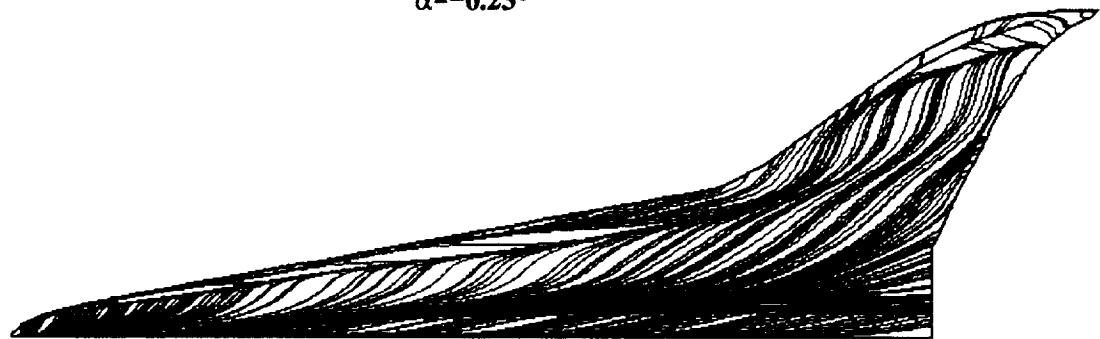


(b) Model station 1.72 and Butt Line .50

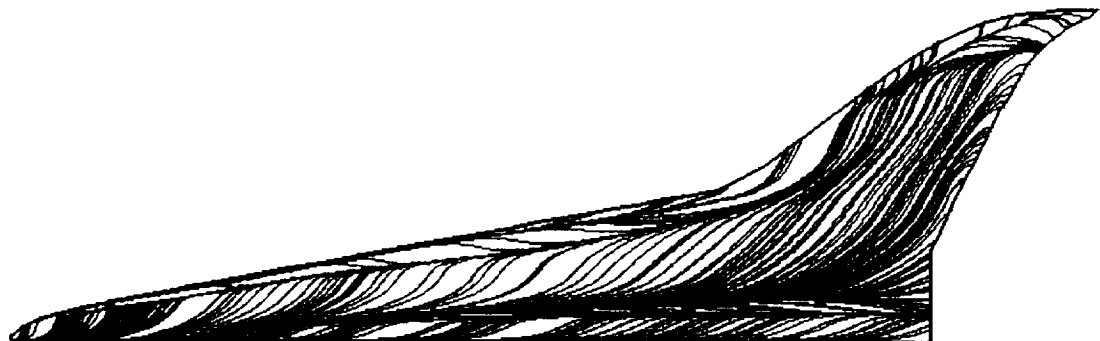
Figure 9. Concluded.



$\alpha = -0.23^\circ$



$\alpha = 10.14^\circ$



$\alpha = 17.78^\circ$

Figure 10. Limiting streamlines on the upper surface of the HSCT model.

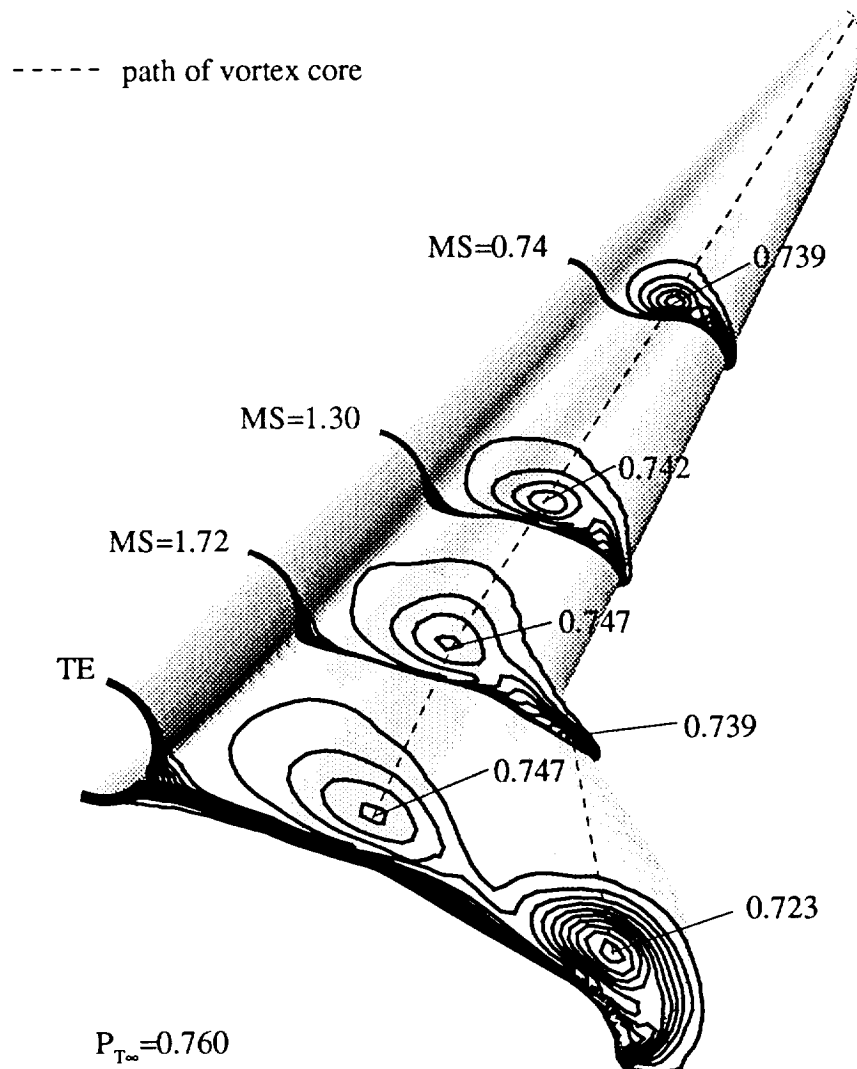


Figure 11. Predicted off-body normalized total pressure contours  
for  $\alpha=5.82^\circ$ .

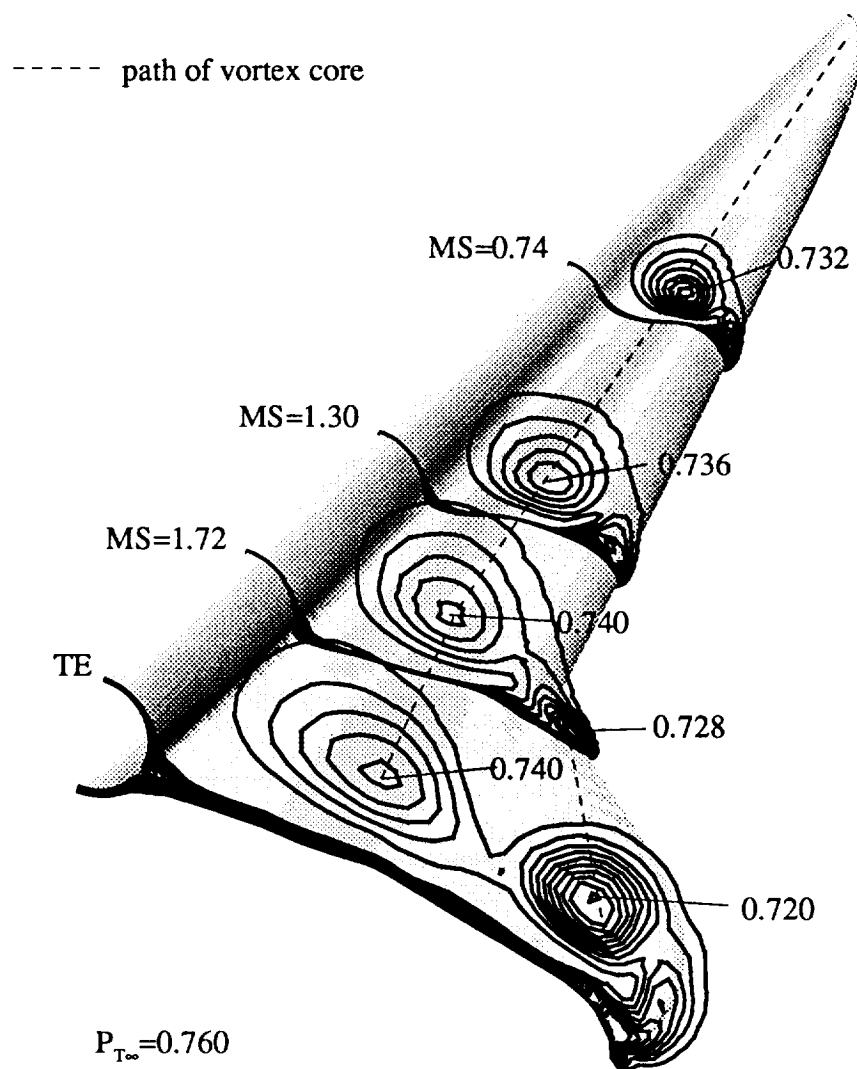


Figure 12. Predicted off-body normalized total pressure contours  
for  $\alpha=10.14^\circ$ .

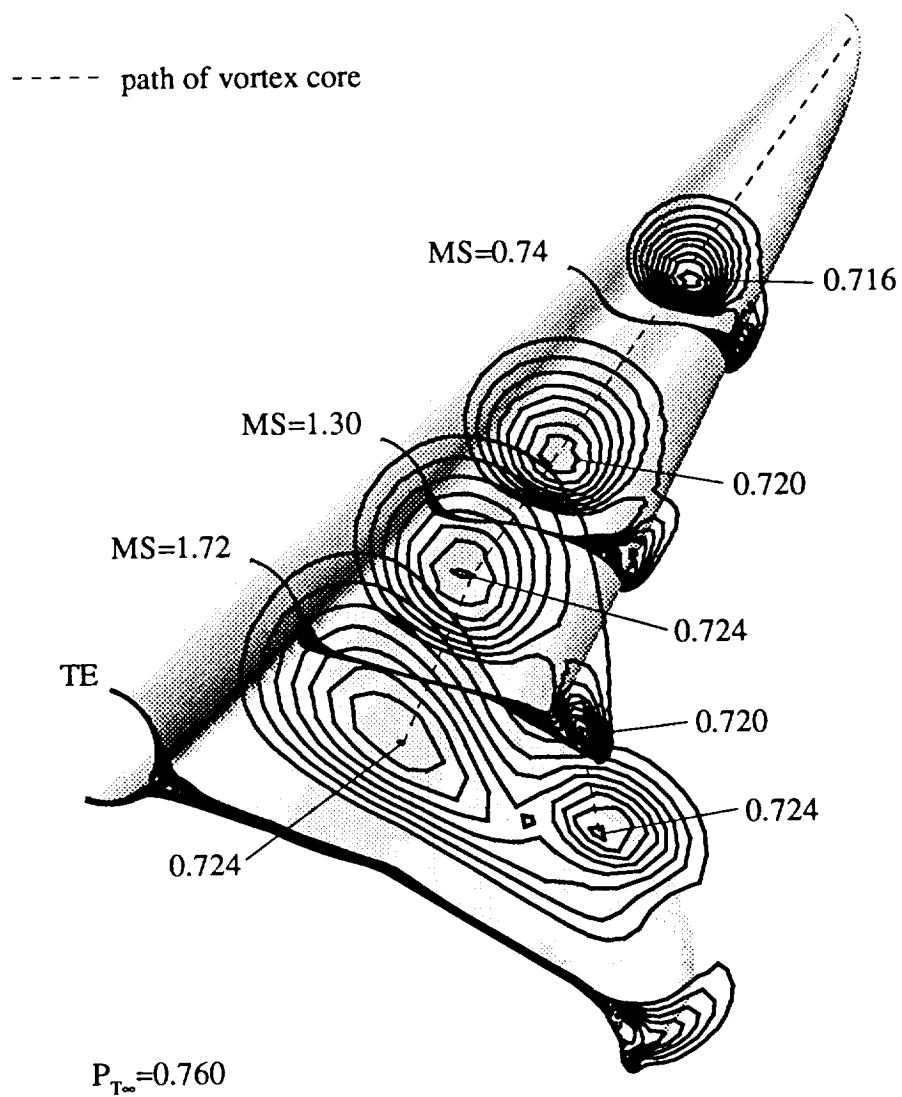


Figure 13. Predicted off-body normalized total pressure contours  
for  $\alpha=17.78^\circ$ .

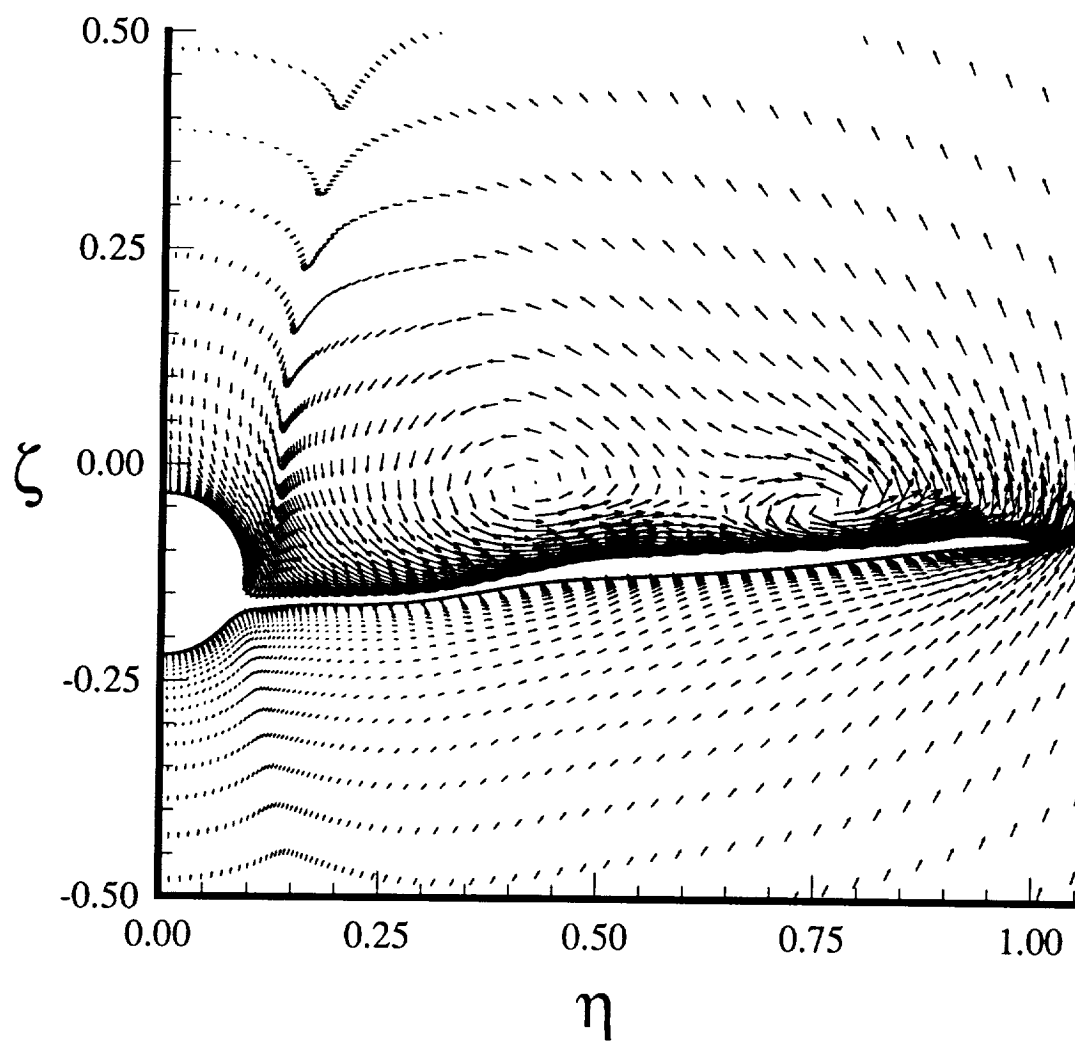


Figure 14. Predicted crossflow velocity vectors at  $MS=1.92$  for  $\alpha=5.82^\circ$ .

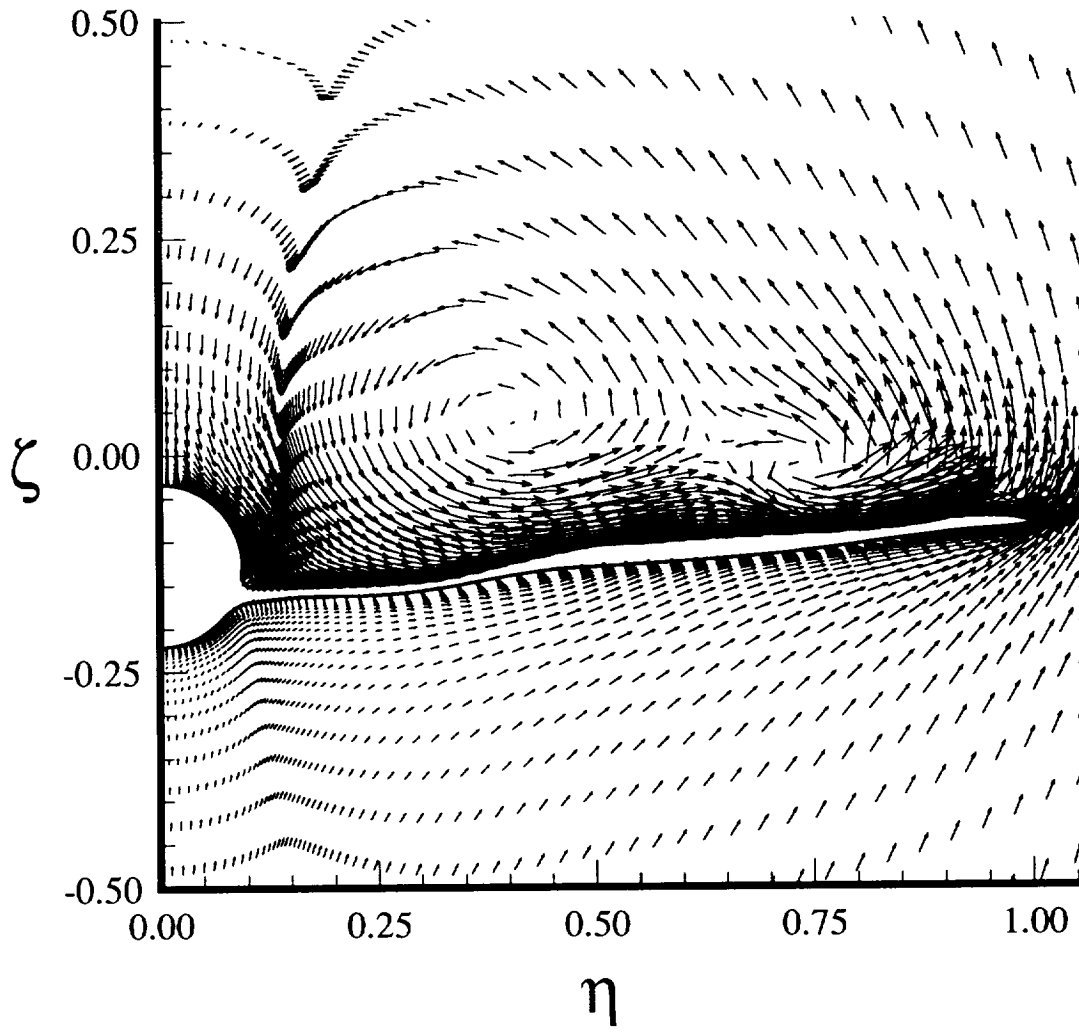


Figure 15. Predicted crossflow velocity vectors at  $MS=1.92$  for  $\alpha=10.14^\circ$ .

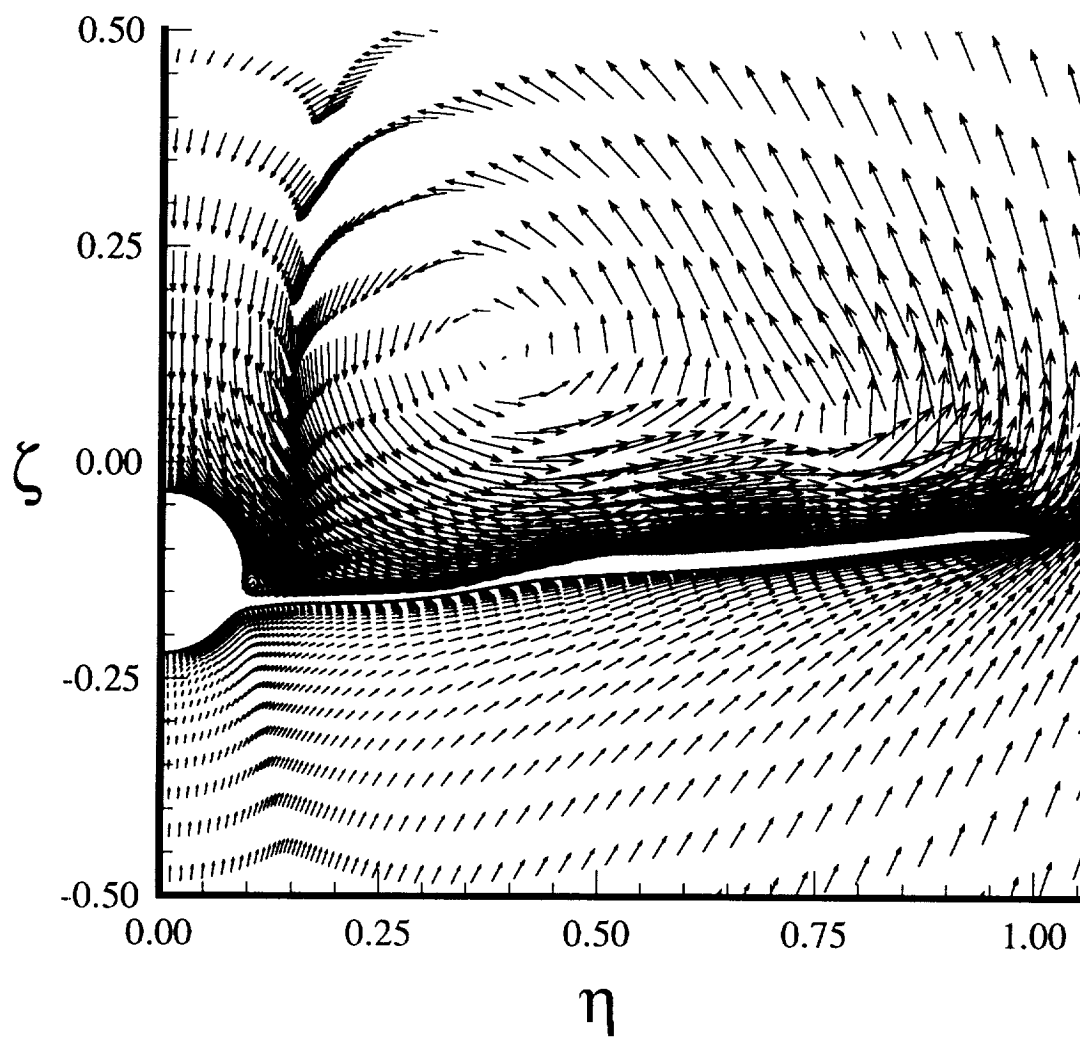


Figure 16. Predicted crossflow velocity vectors at  $MS=1.92$  for  $\alpha=17.78^\circ$ .